A Novel Two-Mode Inverter-Based Open-Winding PMSM Drive and Its Modulation Strategies

Tao Xu, *Student Member, IEEE*, Xueqing Wang, *Member, IEEE*, Dianxun Xiao, *Member, IEEE*, Xin Meng, *Member, IEEE*, Yao Mao, *Member, IEEE*, and Zheng Wang, *Senior Member, IEEE*

***Abstract*—A novel two-mode inverter-based open-winding permanent magnet synchronous motor drive is proposed in this article. The proposed drive operates in hybrid-inverter mode at low and medium speed to achieve high power quality. The common dc-bus mode is adopted at high speed to fulfill a wider speed range than hybrid-inverter mode. Based on the proposed drive, a modulation strategy for any voltage ratio is proposed, which integrates the instantaneous floating capacitor (FC) voltage into modulation to synthesize the reference voltage vector. The proposed modulation strategy can not only guarantee the FC voltage regulation but also start the drive when the FC voltage is zero and switch the mode of the drive smoothly. Besides, the excellent fault-tolerant capability of the proposed drive is studied under open-phase and switch faults. In the proposed fault-tolerant control, a sinusoidal zero-sequence current is injected to tolerate the open-phase fault in the common dc-bus mode and redundant switching combinations are used to tolerate switch faults in the hybrid-inverter mode. All the claimed advantages have been validated by experimental results.**

***Index Terms*—Fault-tolerant control, floating capacitor (FC), modulation strategy, open-winding permanent magnet synchronous motor (OW-PMSM), zero-sequence current (ZSC).**

I. Introduction

With the further development of the automotive industry, electric vehicles are moving towards greater power output and higher reliability [1], [2], [3]. Since the open-winding motor drive was proposed, it has attracted extensive attention of academia and industry [4], [5], [6]. Compared with the conventional permanent magnet synchronous motor (PMSM), the open-winding permanent magnet synchronous motor (OW-PMSM) opens the neutral point of the stator winding, which can achieve a greater power rating and higher reliability [7].

There are three sorts of typical topologies of OW-PMSM drives: Namely common dc-bus topology, isolated dc-bus topology, and hybrid-inverter topology. For OW-PMSM drive with common dc bus, it has a wide speed range and more degrees of freedom in current control but it needs to suppress the zero-sequence current (ZSC) [8], [9]. Besides, it will be difficult to suppress the ZSC when a switch fault occurs if no auxiliary circuit is used [10]. For the OW-PMSM drive with two isolated dc buses, the ZSC path no longer exists and it can achieve a four-level output at the voltage ratio of 2:1, which has excellent power quality [11]. However, the two dc sources of this drive increase system cost and cannot handle open-phase fault due to its limited degrees of freedom in current control. For hybrid-inverter OW-PMSM drive, it can realize four-level output more cheaply as one of the dc sources is replaced by a floating capacitor. Nevertheless, the floating capacitor (FC) voltage must be regulated and the speed range is relatively low compared with OW-PMSM drive with common dc bus [12], [13], [14]. Besides, the typical topologies of OW-PMSM drives can be equipped with auxiliary circuits to further improve the performance and flexibility of OW-PMSM drives [10], [15].

The commonly used voltage ratios of OW-PMSM drives are 1:1 and 2:1. For the voltage ratio of 1:1, the space vector diagram has more redundant switching combinations in each vertex compared with that at the voltage ratio of 2:1 [16], [17], which makes it stronger to deal with faults. For the voltage ratio of 2:1, it is usually applied on the OW-PMSM drive with two isolated buses and hybrid-inverter OW-PMSM drive [18], [19]. In [20], a decoupled space vector modulation strategy was used to realize four-level output in a dual-inverter system at the voltage ratio of 2:1. In [21], the inverter with lower dc voltage was clamped and the other inverter is switched around it in the modulation of the OW-PMSM drive with two isolated dc buses at the voltage ratio of 2:1. To take advantage of the full potential of the OW-PMSM drive, both voltage ratios 1:1 and 2:1 were used by controlling the FC voltage actively in [22]. Nevertheless, in the switching process of voltage ratio, the modulation mismatch will appear because of the unfixed voltage ratio, which will cause undesired torque ripple. So far, a modulation strategy applicable to any voltage ratio of the hybrid-inverter OW-PMSM drive has not been found.

In terms of the fault-tolerant control of the OW-PMSM drive, there are the following three common faults:

Manuscript received 10 November 2022; revised 9 March 2023; accepted 10 April 2023. Date of publication 14 April 2023; date of current version 19 May 2023. This work was supported in part by the Science and Technology Projects of Sichuan Province under Grant 2019ZDZX0019, in part by the Natural Science Foundation of Sichuan Province under Grant 2022NSFSC1888, and in part by the Project of Hetao Shenzhen-Hong Kong Science and Technology Innovation Cooperation Zone under Grant HZQB-KCZYB-2020083. Recommended for publication by Associate Editor S. Panda. *(Corresponding authors: Xueqing Wang; Xin Meng.)*

Tao Xu, Xueqing Wang, and Xin Meng are with the College of Electrical Engineering, Sichuan University, Chengdu 610065, China (e-mail: taolinton@qq.com; wangxueqing231@163.com; mengxin_pe@163.com).

Dianxun Xiao is with Sustainable Energy and Environment Thrust, The Hong Kong University of Science and Technology (Guangzhou), Guangzhou 511455, China, and also with HKUST Shenzhen-Hong Kong Collaborative Innovation Research Institute, Shenzhen 518048, China (e-mail: dianxunxiao@ust.hk).

Yao Mao is with the Key Laboratory of Optical Engineering, Chinese Academy of Sciences, Chengdu 610209, China (e-mail: maoyao@ioe.ac.cn).

Zheng Wang is with the School of Electrical Engineering, Southeast University, Nanjing 210096, China (e-mail: zwang@eee.hku.hk).

Color versions of one or more figures in this article are available at https://doi.org/10.1109/TPEL.2023.3267064.

Digital Object Identifier 10.1109/TPEL.2023.3267064

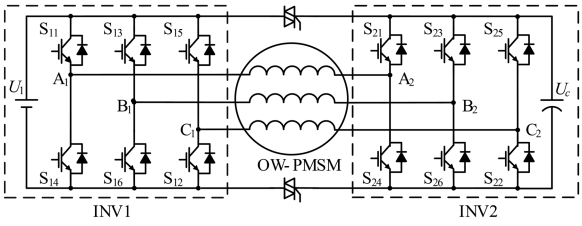

Fig. 1. Proposed two-mode inverter-based OW-PMSM drive.

1) open-phase fault;
2) open-switch fault;
3) short-switch fault.

For the open-phase fault of the OW-PMSM drive, nearly all fault-tolerant control strategies are studied on the basis of common dc-bus topology [10], [23], [24], [25], but this topology is weak to handle single switch faults, especially single switch short-circuit fault. For the open-switch fault and short-switch fault, the OW-PMSM with two isolated dc buses and hybrid-inverter OW-PMSM drive are usually adopted [26], [27], [28]. However, they can hardly cope with the open-phase fault due to their limited degrees of freedom in current control. So far, an OW-PMSM drive that can handle not only the open-phase fault, but also the open-switch fault and short-switch fault has been seldom studied.

Unlike the existing studies, this article proposed a novel two-mode inverter-based OW-PMSM drive, which can guarantee both high power quality and wide speed range. Then, a modulation strategy with any voltage ratio is developed for the proposed OW-PMSM drive. It can balance the FC voltage and avoid modulation mismatch. Besides, the excellent fault-tolerant capability of the proposed drive is explored. On the basis of the proposed modulation strategy, a zero-sequence current injection method is designed to tolerate the open-phase fault in the common dc-bus mode and redundant switching combinations are used to tolerate switch faults in the hybrid-inverter mode.

The rest of this article is organized as follows. The proposed two-mode inverter-based OW-PMSM drive and controlling method are described in Section II. The corresponding detailed modulation strategies for different working conditions are presented in Section III. The fault-tolerant control strategies of open-phase, open-switch, and short-switch faults are proposed in Section IV. The experimental validation is presented in Section V. Finally, Section VI concludes the article.

II. Drive and Control

A. Proposed Two-Mode Inverter-Based OW-PMSM Drive

To fully exploit the potential of the OW-PMSM drive, a novel two-mode inverter-based drive is proposed, as shown in Fig. 1. The voltage ratio is defined as the ratio of the dc source voltage U_1 and the FC voltage U_c. For example, the voltage ratio of 2:1 means that the FC voltage is $U_1/2$ and the voltage ratio of 1:1 means that the FC voltage is U_1.

In normal operation, the size of the space vector diagram at the voltage ratio of 2:1 is smaller than the case of 1:1 and the FC voltage regulation is needed in the hybrid-inverter mode. As a result, the modulation range of hybrid-inverter mode at the voltage ratio of 2:1 is limited, causing a limited speed range. Nevertheless, the proposed drive at the voltage ratio of 2:1 can realize four-level output, which contributes to higher power quality. Thus, the two bidirectional thyristors in Fig. 1 are turned OFF to make the system work in hybrid-inverter mode at voltage ratio of 2:1 when the OW-PMSM operates at low and medium speed. When the OW-PMSM is going to operate at high speed, the capacitor voltage U_c will be charged to the dc source voltage U_1 first. Once it reaches the dc source voltage, the two bidirectional thyristors in Fig. 1 will be turned ON to make the system operate in the common dc-bus mode to achieve a wider speed range. In this way, turning ON the bidirectional thyristors will not result in voltage mismatch or large charging current of the capacitor.

TABLE I
System Mode Selections of Each Working Condition

Conditions	Normal operation		Fault-tolerant operation	
	Low/medium speed	High speed	Open-phase fault	Switch faults
Mode	Hybrid-inverter	Common dc-bus	Common dc-bus	Hybrid-inverter
Voltage ratios	2:1	1:1	1:1	1:1

As for the fault-tolerant operation, when an open-phase fault occurs in the proposed two-mode inverter-based drive, a ZSC needs to be injected [24]. Thus, the two bidirectional thyristors in Fig. 1 should be turned ON to make the system operate in the common dc-bus mode. When an open-switch or short-switch fault occurs, the two bidirectional thyristors need to be turned OFF because the ZSC can hardly be controlled while synthesizing the reference voltage with reduced vectors in the common dc-bus mode. In summary, the system mode selections of each working condition are listed in Table I.

B. Control Framework

The control diagram of the proposed OW-PMSM drive is shown in Fig. 2. The main work of this article is the proposed modulation strategy for any voltage ratio, which is highlighted in cyan in the control diagram. The proposed modulation strategy covers all operating conditions of the proposed OW-PMSM drive, including starting, low speed, high speed, and fault tolerance. To this end, the modulations in both hybrid-inverter mode with 2:1, 1:1, and varying voltage ratios and common dc-bus mode have been intensively studied in this article. The FC voltage regulation has been also included in the proposed modulation strategy to balance the FC voltage and fulfill mode switching. In the aspect of current control, the d-axis current reference i_d^* is set to zero to guarantee high efficiency. As for the 0-axis current control, in order to realize both dc reference tracking in normal operation and ac reference tracking in open-phase fault-tolerant operation, the PI controller is paralleled with a repetitive controller. The 0-axis current reference i_0^*

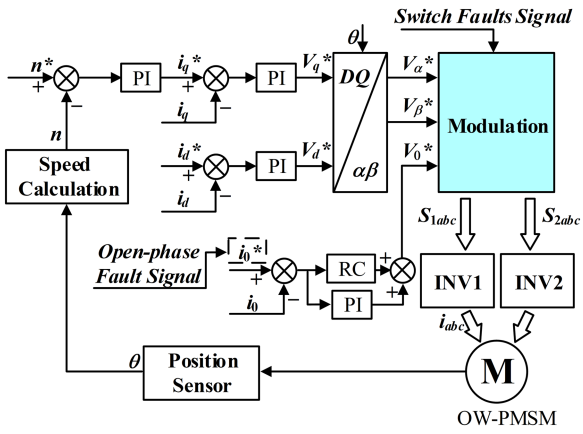

Fig. 2. Control block diagram of the two-mode OW-PMSM drive.

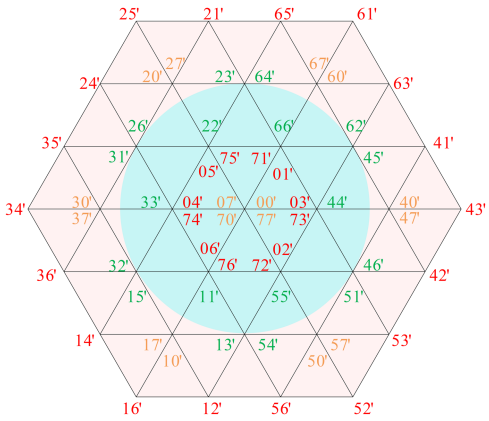

Fig. 3. Space vector diagram at the voltage ratio of 2:1.

will be modified once an open-phase fault is detected and the modulation strategy will change when switch faults occur.

III. Modulation in Normal Operation

In this section, the proposed modulation strategy for any voltage ratio of the proposed OW-PMSM drive will be introduced in detail. Firstly, the modulation of fixed voltage ratios in the hybrid-inverter mode is introduced, namely 2:1 and 1:1, which are developed for the low-speed operation and fault-tolerant operation of switch faults, respectively. Then, the modulation of unfixed voltage ratios in the hybrid-inverter mode is proposed, which can tackle the modulation mismatch when the voltage ratio varies. At last, the modulation of the common dc-bus mode is studied to control the ZSC in normal operation and fault-tolerant operation of open-phase fault.

A. Modulation at the Voltage Ratio of 2:1

To regulate the FC voltage in hybrid-inverter mode, the charging and discharging effect of each voltage vector is fully utilized, which are analyzed in Fig. 3. The numbers in Fig. 3 indicate the switching status of the dual inverter. For instance, the switching combination 62′ is composed of 6(110) from INV1 and 2′(010) from INV2. The red switching combinations discharge the FC, while the green ones charge the FC and the yellow ones hold

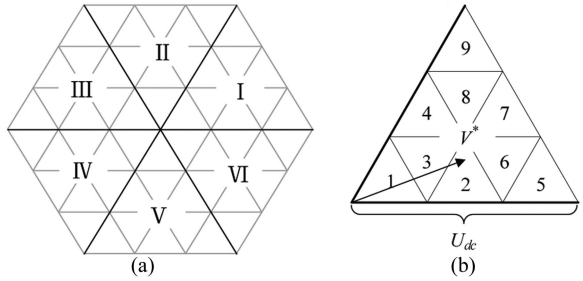

Fig. 4. Sector and subsector dividing at the voltage ratio of 2:1. (a) Sector dividing. (b) Subsector dividing.

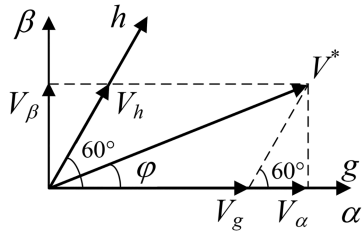

Fig. 5. Projection of V^* in the g-h coordinate system.

the FC voltage [13]. When the FC voltage is lower than its reference, the green switching combinations are selected in the modulation. Otherwise, the red ones are selected. The yellow ones are selected in the case that some required vertexes only have this kind of switching combinations. Based on the above analysis, the cyan circle in Fig. 3 is the effective modulation range that can guarantee circular rotating voltage output and FC voltage regulation since there are both charging and discharging switching combinations in each subsector.

It can be found from Fig. 3 that the drive at the voltage ratio of 2:1 can realize four-level output, which has higher power quality than three-level output. However, its modulation range is limited in the cyan circle and the size of the space vector diagram at the voltage ratio of 2:1 is smaller than that in common dc-bus mode. Therefore, the hybrid-inverter mode at the voltage ratio of 2:1 is applied to low and medium speed.

The sector and subsector dividing are shown in Fig. 4. The space vector diagram, as shown in Fig. 4(a), is divided into six sectors, and each sector is divided into nine subsectors, as shown in Fig. 4(b). The reference voltage V^* is projected into the g- and h-axis to identify the sector and subsector, as shown in Fig. 5. The expressions of g- and h-axis components of V^* can be deduced from Fig. 5, as expressed in (1).

$$\begin{cases} U_{\text{base}} = \frac{2}{3}(U_1 + U_c) \\ U_{\text{dc}} = \frac{U_1}{U_{\text{base}}} \\ V^* = \frac{\sqrt{V_\alpha^2 + V_\beta^2}}{U_{\text{base}}} \\ V_g = V^* \cos\varphi - V_h \cos 60^\circ = V^* \left(\cos\varphi - \frac{\sqrt{3}}{3}\sin\varphi\right) \\ V_h = \frac{V^* \sin\varphi}{\sin 60^\circ} = \frac{2\sqrt{3}}{3} V^* \sin\varphi \end{cases} \tag{1}$$

where U_{base} is the base value of the voltage normalization; U_{dc} is the per-unit value of U_1; V_α and V_β are α- and β-axis

TABLE II
SUBSECTOR IDENTIFICATION AT THE VOLTAGE RATIO OF 2:1

Subsectors	Condition
1	$V_g < 1/3$ & $V_h < 1/3$ & $(V_g + V_h) \le 1/3$
2	$V_g < 2/3$ & $V_h < 1/3$ & $(V_g + V_h) \le 2/3$
3	$V_g < 1/3$ & $V_h < 1/3$ & $(V_g + V_h) > 1/3$
4	$V_g < 1/3$ & $V_h > 1/3$ & $(V_g + V_h) \le 2/3$

components of the reference voltage V^*, respectively; V_g and V_h are g- and h-axis components of V^*, respectively; φ is the angle between V^* and g-axis; V_g, V_h, and V^* are all per-unit values.

The sector of V^* can be identified by calculating the angle of V^* and subsector identification can be fulfilled in the g-h coordinate system based on Fig. 4(b) and (1), as shown in Table II. In Table II, only the cases of Subsectors 1–4 are shown because only in these regions the FC voltage can be regulated at the voltage ratio of 2:1.

After identifying the sector and subsector of V^*, voltage vectors at the nearest triangle vertexes are selected in modulation considering charging or discharging the FC. Then, volt-second balancing equations of synthesizing the reference voltage vector in g-h coordinate systems are constructed to calculate the duration of each vector, as expressed in (2)

$$\begin{cases} V_{1g}T_1 + V_{2g}T_2 + V_{3g}T_3 = V_gT_s \\ V_{1h}T_1 + V_{2h}T_2 + V_{3h}T_3 = V_hT_s \\ T_1 + T_2 + T_3 = T_s \end{cases} \tag{2}$$

where V_{Xg} and V_{Xh} are g- and h-axis components of selected vector X ($X = 1, 2, 3$), respectively; T_X is the corresponding duration of voltage vector X; and T_s is the switching period.

It is noteworthy that using the volt-second balancing principle to center the durations of high voltage levels of each leg directly is forbidden because it will change the switching combinations and the charging or discharging effect of the FC. Besides, if the sequence of selected switching combinations remains unchanged, the undesired switching loss caused by the disorganized sequence will appear. Thus, to minimize the switching loss, the sequence of selected switching combinations is optimized to make the high voltage levels of each leg locate in the center of a switching period as much as possible without changing the switching combinations, as shown in Fig. 6. It can be found from Fig. 6 that the switching combinations and their durations remain unchanged before and after the switching sequence optimization.

B. Modulation at the Voltage Ratio of 1:1 in Hybrid-Inverter Mode

Modulation at the voltage ratio of 1:1 in hybrid-inverter mode is similar to that of 2:1. The space vector diagram and the subsector dividing at the voltage ratio of 1:1 are shown in Figs. 7 and 8, respectively. The sector dividing follows the same rules as the case of 2:1 but the subsector identification is simpler as only Subsector 1 can guarantee the FC voltage regulation. After the sector and subsector are identified, the voltage vector selection,

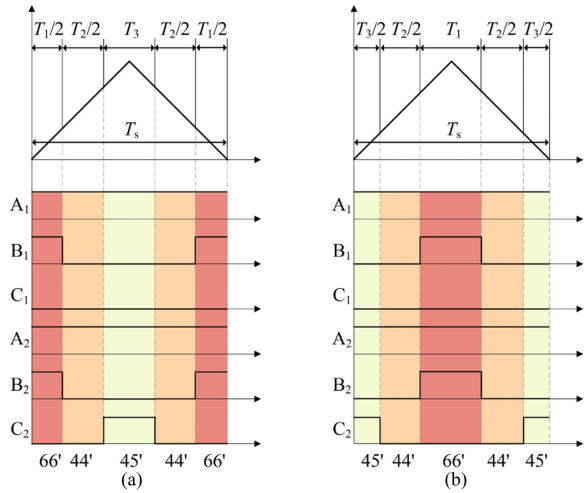

Fig. 6. Sequence optimization of selected switching combinations. (a) Before optimization. (b) After optimization.

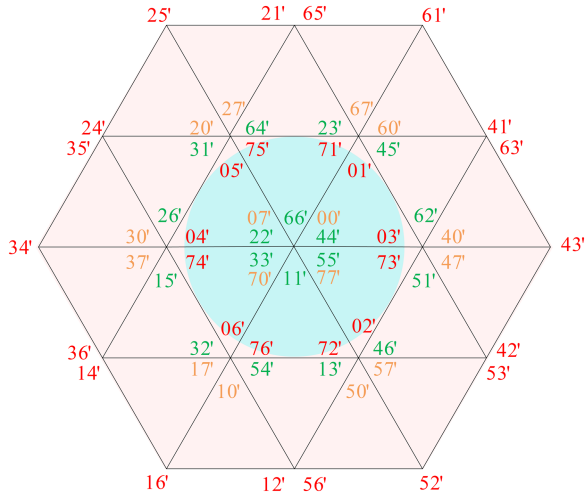

Fig. 7. Space vector diagram at the voltage ratio of 1:1.

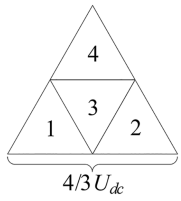

Fig. 8. Subsector dividing at the voltage ratio of 1:1.

the vector durations calculation, and the operation sequence optimization can be fulfilled in the same way as Section III-A. It should be noted that the size of the cyan circle in Fig. 7 is the same as that in Fig. 3 because the size of the circumscribed hexagon of the cyan circle only depends on the constant U_1 of INV1. Thus, the proposed two-mode inverter-based open-winding PMSM drive in hybrid-inverter mode shares the same speed range with the standard star-connected three-phase PMSM drive when powered by the same dc voltage source. Once U_c rises to U_1, the bidirectional thyristors will be turned ON to make the system switch into common dc-bus mode. In fault-tolerant operations,

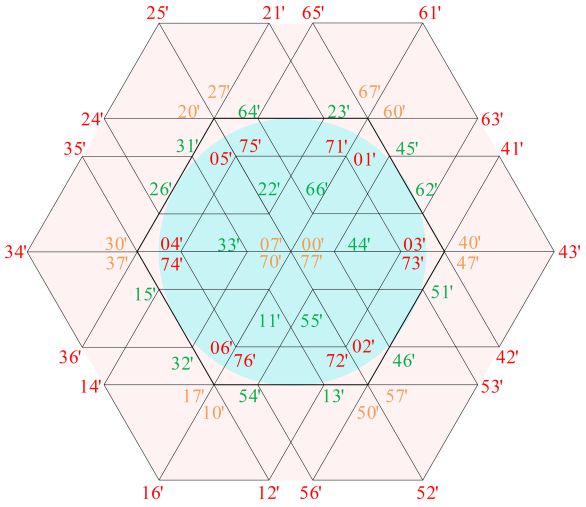

Fig. 9. Space vector diagram when the voltage ratio changes from 2:1 to 1:1.

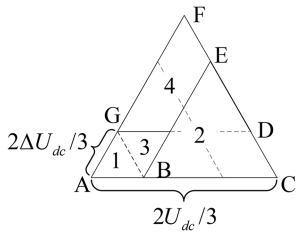

Fig. 10. Subsector dividing when the voltage ratio changes from 2:1 to 1:1.

the redundant switching combinations at the 1:1 voltage ratio in hybrid-inverter mode are used to tolerate the open-switch fault and short-switch fault.

C. Modulation at the Voltage Ratio Between 2:1 and 1:1

The FC needs to be charged when the voltage ratio changes from 2:1 to 1:1. If the modulation strategy remains unchanged, both the synthesis of the reference voltage and the regulation of capacitor voltage will be affected. The space vector diagram and subsector dividing at the voltage ratios between 2:1 and 1:1 are shown in Figs. 9 and 10, respectively.

Only the cyan circle-covered hexagon regions of Fig. 9 are divided in Fig. 10 and the variable $\Delta U_{\rm dc}$ in Fig. 10 is used to identify the subsector of V^*, as defined in (3)

$$\Delta U_{\rm dc} = \frac{(U_1 - U_c)}{U_{\rm base}} \tag{3}$$

where $\Delta U_{\rm dc}$ is the per-unit voltage difference between the dc source and the FC. It is worthwhile mentioning that $\Delta U_{\rm dc}$ will decrease and the size of Fig. 9 will grow as U_c is increasing. Therefore, this modulation strategy is a universal one for any voltage ratio between 2:1 and 1:1.

Based on Fig. 10 and (3), subsector identification can be fulfilled in the *g*-*h* coordinate system, as shown in Table III. In Fig. 10, Subsectors 1, 2, and 3 are all triangles and Subsector 4 is a trapezoid. The vectors A, B, and G are selected when V^* is located in Subsector 1 and the vectors B, C, and E are selected when V^* is located in Subsector 2. When V^* is located in Subsector 3, vectors G, B, and E are selected and the vectors G, D, and F are selected when V^* is located in subsector 4, as shown in Table III. Then, the duration calculating and sequence optimization at the voltage ratios between 2:1 and 1:1 can be implemented in the same way as Section III-A.

TABLE III
SUBSECTOR IDENTIFICATION AT THE VOLTAGE RATIO BETWEEN 2:1 AND 1:1

Subsector	Condition	Vectors
1	$V_g \le 3\Delta U_{dc}/2$ & $V_h \le 3\Delta U_{dc}/2$ & $(V_g + V_h) \le 3\Delta U_{dc}/2$	ABG
2	$V_g > 3\Delta U_{dc}/2$	BCE
3	$V_g \le 3\Delta U_{dc}/2$ & $V_h \le 3\Delta U_{dc}/2$ & $(V_g + V_h) > 3\Delta U_{dc}/2$	GBE
4	*else*	GDF

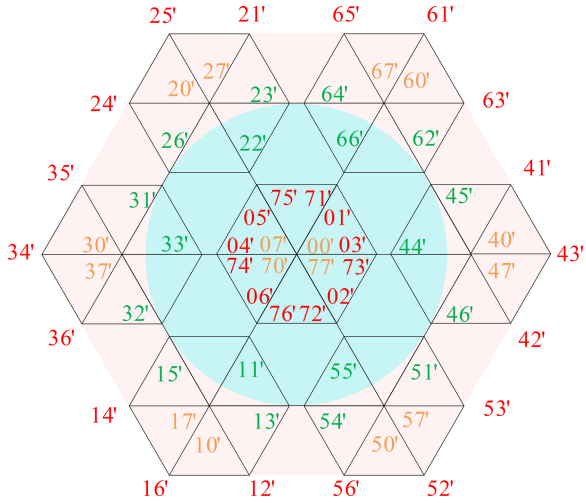

Fig. 11. Space vector diagram at motor starting.

D. Modulation at the Voltage Ratios Between 2:0 and 2:1

In the startup process, the voltage ratio is between 2:0 and 2:1. The modulation of motor starting is similar to that when the voltage ratio changes from 2:1 to 1:1 because both voltage ratios are unfixed. It is worth mentioning that the voltage ratio of 2:0 only appears when the drive starts. At this moment, the line voltages of INV2 are all zero with any voltage vector, which means INV2 automatically forms a neutral point of the OW-PMSM. In the starting process, the FC voltage will increase gradually, the voltage ratio will change from 2:0 to 2:1 accordingly. In summary, instead of actively controlling the drive to the ratio of 2:0, the proposed strategy guarantees precise vector generation by automatically accommodating the unfixed voltage ratio during the transition of FC voltage.

The space vector diagram and subsector dividing of the motor starting are shown in Figs. 11 and 12, respectively. The calculation of $U_{\rm dc}$ and $\Delta U_{\rm dc}$ are shown in (1) and (3), respectively. The subsector identification and vector selection table are shown in

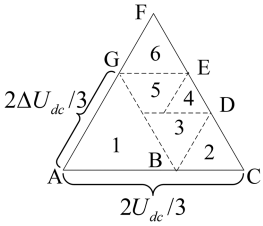

Fig. 12. Subsector dividing at motor starting.

TABLE IV
SUBSECTOR IDENTIFICATION AT THE VOLTAGE RATIO BETWEEN 2:0 AND 2:1

Subsector	Condition	Vectors
1	$V_g \le 3\Delta U_{dc}/2$ & $V_h \le 3\Delta U_{dc}/2$ & $(V_g + V_h) \le 3\Delta U_{dc}/2$	ABG
2	$V_g > 3\Delta U_{dc}/2$	BCD
3	$V_g \le 3\Delta U_{dc}/2$ & $V_h \le 3(U_{dc} - \Delta U_{dc})/2$ & $(V_g + V_h) > 3\Delta U_{dc}/2$	GBD
4	$V_g > 3(U_{dc} - \Delta U_{dc})/2$ & $V_h > 3(U_{dc} - \Delta U_{dc})/2$ & $(V_g + V_h) \le 3U_{dc}/2$	ADE
6	$V_h > 3(U_{dc} - \Delta U_{dc})/2$	GEF
5	*else*	GBE

Table IV. The vector durations calculation and sequence optimization can be implemented in the same way as Section III-C.

E. Modulation in Common DC-Bus Mode

The space vector diagram of the common dc-bus mode is the same as that at the voltage ratio of 1:1 in hybrid-inverter mode, as shown in Fig. 7. In common dc-bus mode, since the FC is paralleled with the dc source, the modulation range is the inscribed circle of the outer hexagon in Fig. 7, whose radius is twice of the cyan circle in Fig. 7. Therefore, the proposed drive in common dc-bus mode has a nearly double speed range compared with that in hybrid-inverter mode. Nevertheless, due to the zero-sequence path, the ZSC suppression is required in the common dc-bus mode. To handle the ZSC problem, a CMV elimination method is developed to suppress the ZSC caused by the modulation and a ZSC closed-loop control is introduced to further suppress the ZSC caused by the inverter nonlinearity and the harmonics of the back electromotive force.

To better elucidate the CMV elimination, some variables are needed to be defined, which are as follows:

$$\begin{cases} T_{\rm cm} = (T_{1a} + T_{1b} + T_{1c} - T_{2a} - T_{2b} - T_{2c})/3 \\ T_{1\min} = \min\{T_{1a}, T_{1b}, T_{1c}\} \\ T_{1\max} = \max\{T_{1a}, T_{1b}, T_{1c}\} \\ T_{2\min} = \min\{T_{2a}, T_{2b}, T_{2c}\} \\ T_{2\max} = \max\{T_{2a}, T_{2b}, T_{2c}\} \\ T_s = 1/f_s \end{cases} \tag{4}$$

where T_{cm} is the CMV durations; T_{1a}, T_{1b}, and T_{1c} are the three-phase high-level durations of INV1; T_{2a}, T_{2b}, and T_{2c} are three-phase high-level durations of INV2; $T_{1\min}$ and $T_{1\max}$ are the minimum and maximum values of T_{1a}, T_{1b}, and T_{1c}; $T_{2\min}$ and $T_{2\max}$ are the minimum and maximum values of T_{2a}, T_{2b}, and T_{2c}. f_s is the switching frequency.

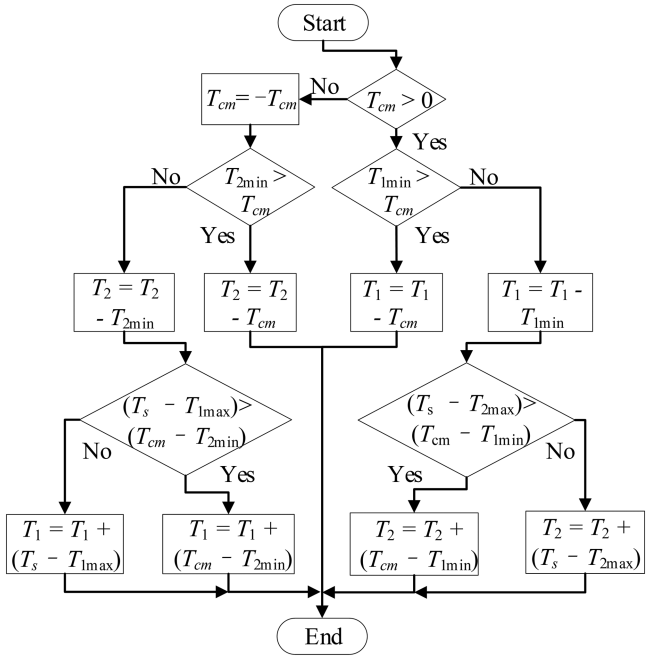

Fig. 13. Flowchart of CMV elimination.

After the preparation of (4), if $T_{\rm cm}$ is positive, the three-phase high-level durations of INV1, which is T_1 in Fig. 13, are added or subtracted to eliminate the CMV durations of voltage vectors firstly. If the CMV durations cannot be eliminated in the first stage, then the three-phase high-level durations of INV2, which is T_2 in Fig. 13, are added or subtracted to eliminate the rest CMV durations. If $T_{\rm cm}$ is negative, the elimination is similar to that when $T_{\rm cm}$ is positive. The detailed process of common-mode voltage elimination is shown in Fig. 13. It is noteworthy that changing $T_{\rm cm}$ to $-T_{\rm cm}$ will make the common voltage elimination become injection, which will be used to realize the ZSC closed-loop control in Section IV-A.

The complete modulation strategy in the whole working process is shown in Fig. 14. The system operates in the hybrid-inverter mode of voltage ratio 2:1 to achieve high power quality and in the common dc-bus mode to realize a wide speed range. When the motor starts or the voltage ratio changes from 2:1 to 1:1, the proposed strategy for any voltage ratio is used to make the FC voltage rise smoothly without modulation mismatch.

The simulation results of the FC voltage, the FC current, and motor speed in full operating conditions are shown in Fig. 15. It can be seen from Fig. 15 that the proposed modulation strategy at the voltage ratio between 2:0 and 2:1 can charge the FC and start the motor smoothly. As soon as the FC voltage reaches half of the dc source, the drive switches to the hybrid-inverter mode and the modulation strategy at the voltage ratio of 2:1 is applied to regulate the FC voltage, which is magnified at the lower right of Fig. 15. To present all the normal operating conditions, the reference voltage ratio of the proposed drive is

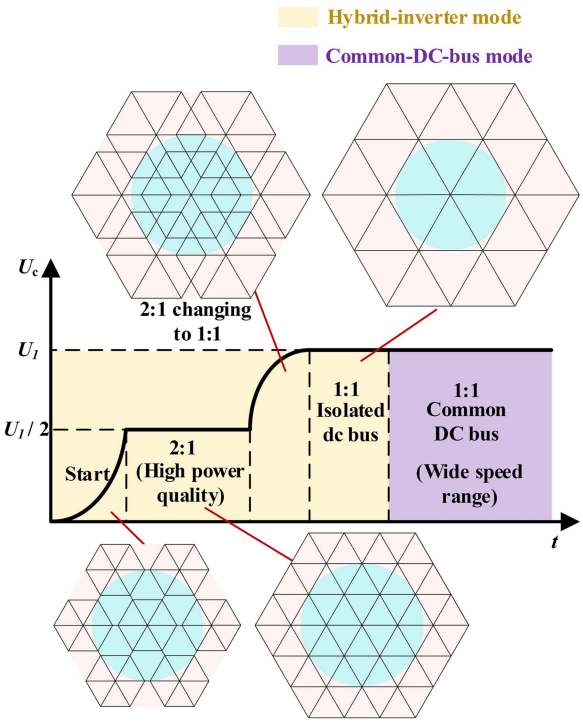

Fig. 14. Summary of all the modulation processes.

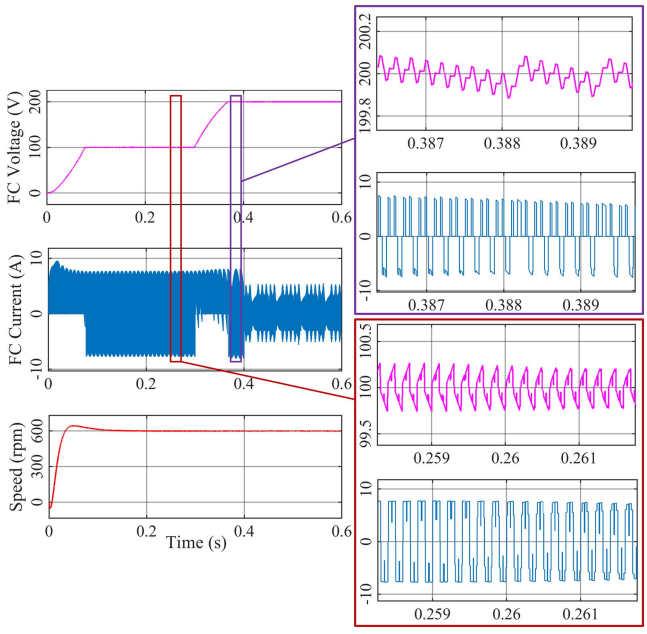

Fig. 15 Simulation results of the normal operation.

set to 1:1 at $t = 0.3$. After this instant, the proposed modulation strategy at the voltage ratio between 2:1 and 1:1 is applied to make the FC voltage increase to the dc source voltage while keeping the speed stable. As soon as the FC voltage reaches the dc source voltage, the modulation strategy at the voltage ratio of 1:1 is applied and it can be found from the upper right of Fig. 15 that the FC voltage has been balanced effectively. When $t = 0.4$, the two bidirectional thyristors are turned ON to make the drive switch to the common dc-bus mode with the ZSC suppression strategy applied. In the whole process, the motor speed rises smoothly and remains stable whether the FC voltage varies or not, which shows excellent performance of the proposed modulation strategy for any voltage ratio.

IV. Fault-Tolerant Control

A. Open-Phase Fault

In this article, a novel zero-sequence injection-based fault-tolerant control is proposed for the open-phase fault of the OW-PMSM drive without reshaping the space vector diagram. The Phase-A open-phase fault will be presented as an example.

The phase current references with zero d-axis current are

$$\begin{cases} i_a^* = I_q^* \cos\left(\omega t + \frac{\pi}{2}\right) \\ i_b^* = I_q^* \cos\left(\omega t - \frac{\pi}{6}\right) \\ i_c^* = I_q^* \cos\left(\omega t + \frac{7\pi}{6}\right) \end{cases} \tag{5}$$

where I_q^* is the amplitude of the q-axis current reference.

To deduce the fault-tolerant 0-axis current reference, the relations between phase currents and α-, β-, and 0-axis currents are established according to the inverse Clark transform

$$\begin{cases} i_a^* = i_\alpha^* + i_0^* \\ i_b^* = -\frac{1}{2} \cdot i_\alpha^* + \frac{\sqrt{3}}{2} \cdot i_\beta^* + i_0^* \\ i_c^* = -\frac{1}{2} \cdot i_\alpha^* - \frac{\sqrt{3}}{2} \cdot i_\beta^* + i_0^* \end{cases} \tag{6}$$

where i_α^*, i_β^*, and i_0^* are α-, β-, and 0-axis current references.

In fault-tolerant operation, constructing equivalent rotating magnetomotive force is the foundation of generating stable torque. Thus, α-axis and β-axis current references should remain unchanged with the zero Phase-A current constraint. Thus, the Phase-A current reference under Phase-A open-phase fault should be set to zero considering the first equation of (5)

$$i_{a\_op}^* = i_{\alpha\_op}^* + i_{0\_op}^* = i_\alpha^* + i_{0\_op}^* = 0 \tag{7}$$

where $i_{a\_op}^*$, $i_{\alpha\_op}^*$, and $i_{0\_op}^*$ are Phase-A current reference, α-axis current reference, and 0-axis current reference under open-phase fault, respectively.

Combining (5), (7), and Clarke transformation, $i*_{0\cdot op}$ can be deduced as

$$i_{0\_op}^* = -i_\alpha^* = -\left(\frac{2}{3}i_a^* - \frac{1}{3}i_b^* - \frac{1}{3}i_c^*\right) = I_q^* \sin(\omega t). \tag{8}$$

By injecting the sinusoidal ZSC in (8), the Phase-A current is actively controlled to zero and the expressions of α-axis and β-axis currents remain unchanged. In this way, the torque fluctuation under open-phase fault can be eliminated.

Combining the inverse Park transformation and (8), the fault-tolerant three-phase current reference for open-phase fault can be obtained as

$$\begin{cases} i_{a\_op}^* = 0 \\ i_{b\_op}^* = \sqrt{3} I_q^* \cos(\omega t - \frac{\pi}{3}) \\ i_{c\_op}^* = -\sqrt{3} I_q^* \cos(\omega t + \frac{\pi}{3}) \end{cases} . \tag{9}$$

It can be deduced from (5) and (9) that the copper loss of OW-PMSM in the fault-tolerant operation of open-phase fault

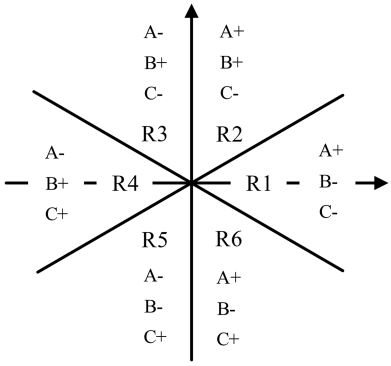

Fig. 16. Current directions at different current vector regions.

TABLE V
CHARGING OR DISCHARGING EFFECTS OF EACH VECTOR

Region	Voltage vectors							
	Y0'	Y1'	Y2'	Y3'	Y4'	Y5'	Y6'	Y7'
R1	=	↓	↓	↓	↑	↑	↑	=
R2	=	↓	↑	↓	↑	↓	↑	=
R3	=	↓	↑	↑	↓	↓	↑	=
R4	=	↑	↑	↑	↓	↓	↓	=
R5	=	↑	↑	↑	↓	↑	↓	=
R6	=	↑	↑	↓	↑	↑	↓	=

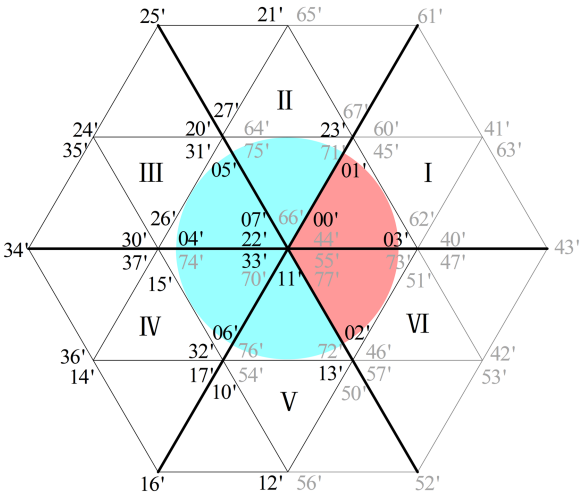

Fig. 17. Space vector diagram of S_{11} open-switch fault.

is double that in normal operation. Besides, the conduction loss of the dual inverter will also increase due to the increase of phase current amplitude. Therefore, in the fault-tolerant operation of open-phase fault, the total loss of OW-PMSM drive will increase and the efficiency will decrease. In the practical application, derating is usually adopted to avoid the overheating problem in the fault-tolerant operation.

TABLE VI
PARAMETERS OF THE OW-PMSM SYSTEM

Symbol	System Parameters	Value
U_r	Rated voltage	220 V
T_{e_r}	Rated load torque	10 Nm
n_r	Rated speed	1500 /min
f_r	Rated current frequency	100 Hz
L_d	d-axis inductance	8.91 mH
L_q	q-axis inductance	17.03 mH
R_s	Stator resistance	1.4 Ω
ψ_f	Permanent magnet flux linkage	0.301 Wb
p	Number of pole pairs	4
U_1	DC bus voltage	200 V
C	Capacitance of the FC	3300 μF

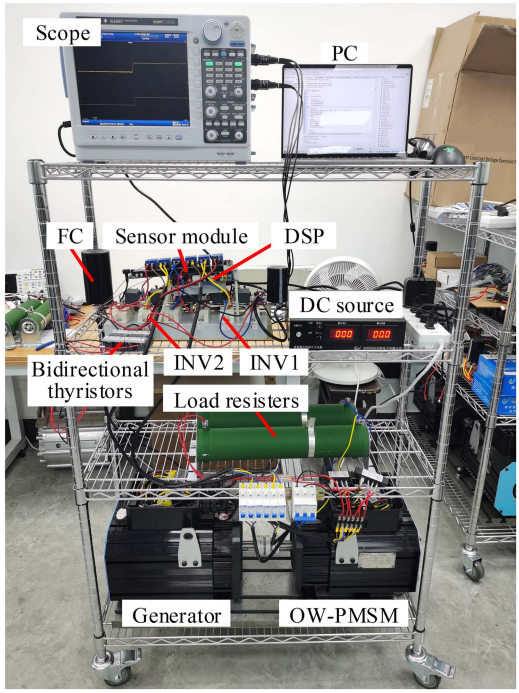

Fig. 18. Experimental platform of the OW-PMSM system.

B. Switch Faults

Switch faults can be classified into open-switch fault and short-switch fault. The proposed two-mode inverter-based drive cannot operate in the common dc-bus mode under the open-switch fault because the ability to suppress common voltage is insufficient, which will cause a large ZSC. Thus, the hybrid-inverter mode will be selected in the fault-tolerant control of open-switch fault.

For the fault-tolerant control of open-switch fault, the FC voltage should also be regulated but more precisely. Considering the winding inductance, whether charging or discharging the FC only depends on the instantaneous current direction and the switching combinations of INV2. The relationship between the current direction and the current vector is shown in Fig. 16. The current space vector diagram is divided into six regions according to the directions of three-phase currents. The "+" in Fig. 16 means the current flows from INV1 to INV2 and the "–"

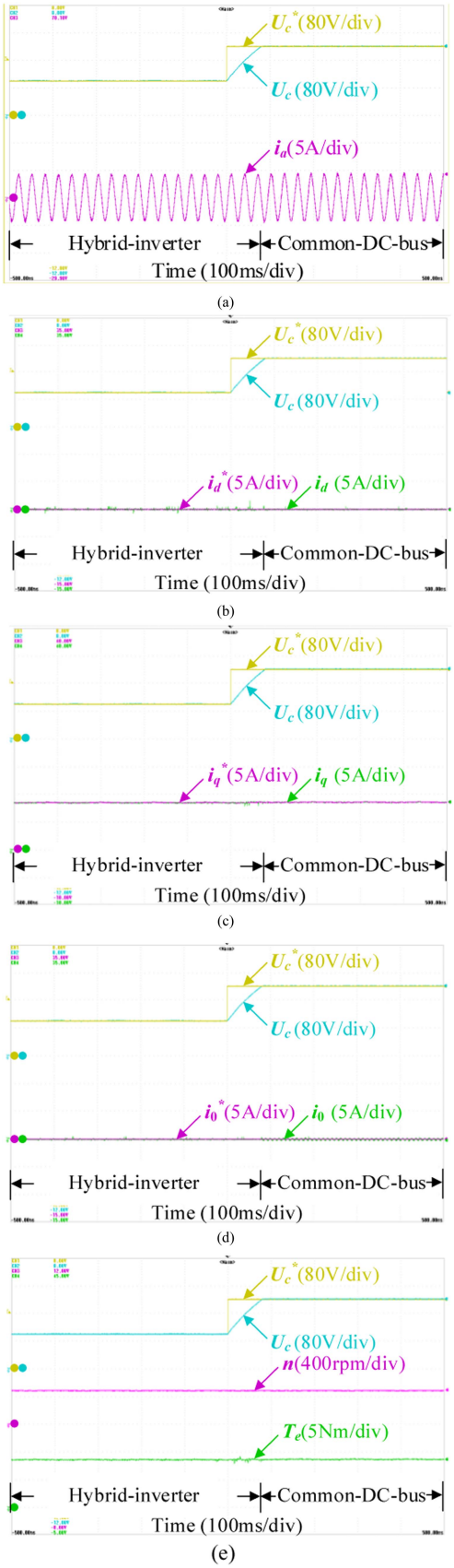

Fig. 19. Normal operation. (a) Floating capacitor voltages and Phase-A current. (b) d-axis currents. (c) q-axis currents. (d) 0-axis currents. (e) Speed and torque.

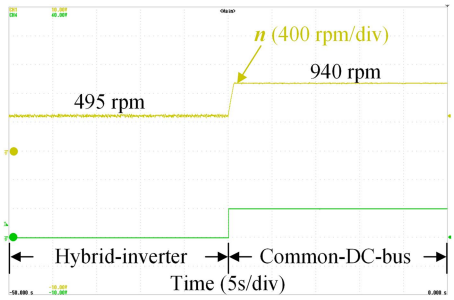

Fig. 20. Comparison of the maximum speed at $U_1 = 100$ V without load.

means the reverse direction. The charge or discharge effect of each voltage vector is shown in Table V. In Table V, "=", "↓", and "↑" means holding on, discharging, and charging the FC voltage, respectively. Y represents the number 0–7. For example, when Y is 6, Y3' represents the switch combination of 63′.

The voltage space vector diagram of S_{11} open-switch fault is shown in Fig. 17. The missing switching combinations are marked in gray and the remaining ones are marked in black. According to Table V, the Sectors II–V can guarantee the FC voltage regulation, which is painted in cyan in Fig. 17. Sector I and Sector VI can only discharge the capacitor, which is painted in red in Fig. 17. Considering that there are only discharging vectors in red sectors, charging vectors are always selected to precharge the FC in Sector V. The rest of the modulation can be implemented in the same way as Section III-B.

For the short-switch fault, when S_{11} short-switch fault occurs, S_{14} is always turned OFF to avoid shooting through the leg. Thus, the space vector diagram of the short-switch fault is the same as that of the open-switch fault in the same leg. Therefore, the modulation strategy of these two faults is designed identically. For instance, the modulation strategy of the S_{11} short-switch fault is designed the same as S_{14} open-switch fault.

As for the efficiency of fault-tolerant operation in switch faults, the three-phase currents are identical to those in normal operation. Thus, the efficiency of the OW-PMSM drive is almost unchanged after entering the fault-tolerant operation of the open-switch fault.

V. Experiment Validation

To validate the effectiveness of the proposed modulation strategy for any voltage ratio and fault-tolerant strategies, the experiments were carried out on a laboratory prototype of the proposed two-mode inverter-based drive. The detailed system parameters are listed in Table VI and the experimental platform is shown in Fig. 18. The OW-PMSM drive is powered by the dc source and the FC. The buses of INV1 and INV2 are connected by the two bidirectional thyristors. The digital signal processor performs the control algorithm and generates drive signals. The OW-PMSM is mechanically coupled to a generator, and the adjustable load resistors are connected to the output of the generator to consume the generated electricity.

The normal operations at a constant 500 r/min speed 8 Nm load are shown in Fig. 19, where the drive switches from hybrid-inverter mode to common dc-bus mode and the FC voltage is

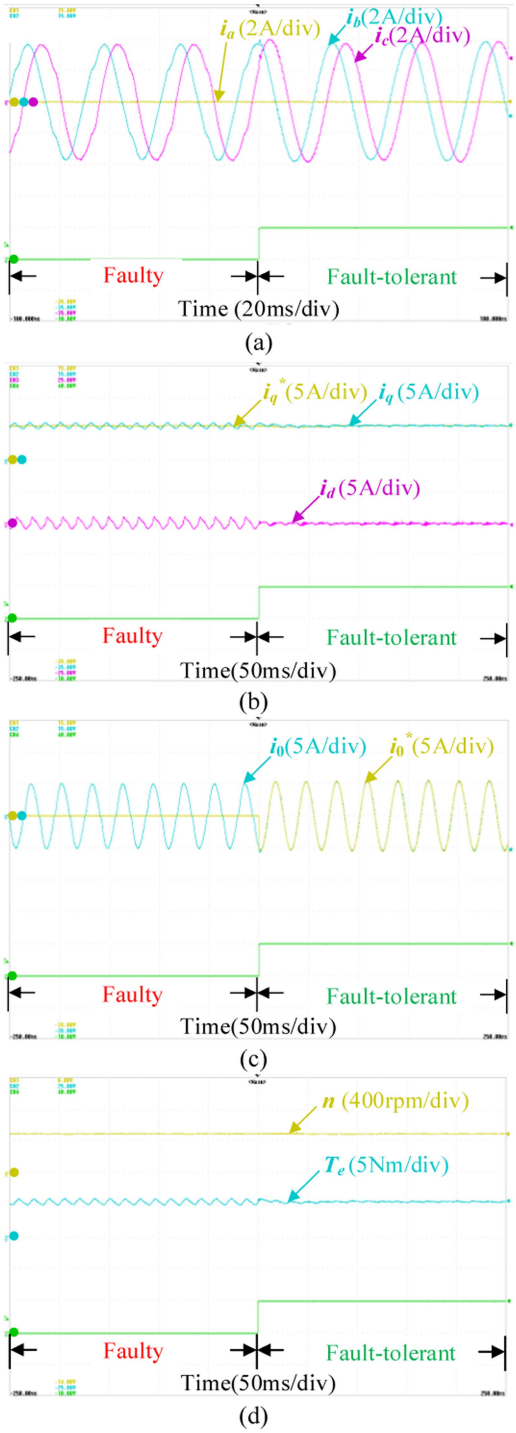

Fig. 21. Fault-tolerant control of Phase-A open-phase fault. (a) Three-phase currents. (b) d-axis and q-axis currents. (c) 0-axis currents. (d) Speed and torque.

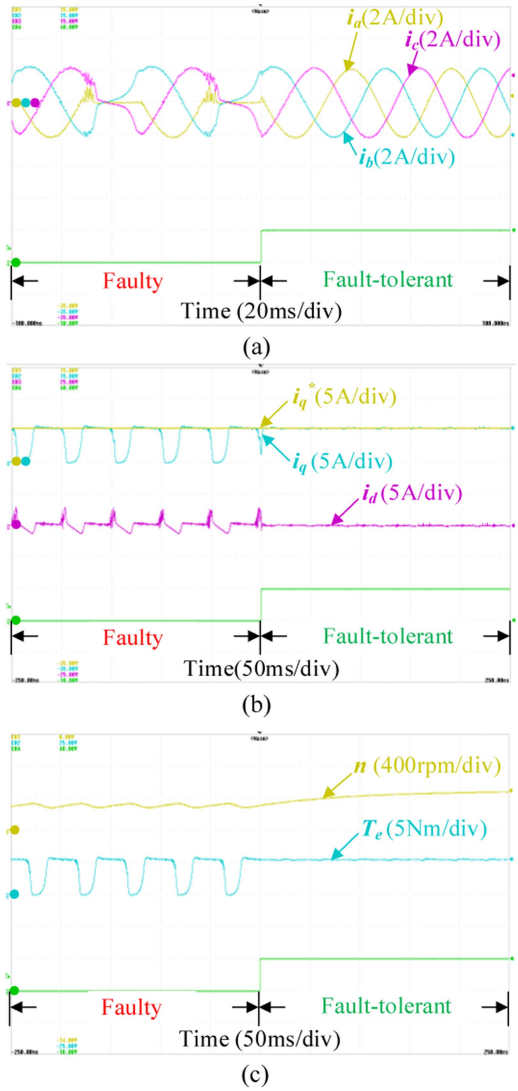

Fig. 22. Fault-tolerant control of S_{11} open-circuit fault. (a) Three-phase currents. (b) d-axis and q-axis currents. (c) Speed and torque.

charged from $U_1/2$ to U_1. In Fig. 19(a), the THD of the phase current is 2.36% at the voltage ratio of 2:1 in hybrid-inverter mode, while it is 3.17% in common dc-bus mode, which proves the high power quality of hybrid-inverter mode at the voltage ratio of 2:1. The THD differences mainly stem from the spectrum near the switching frequency, as expected. It can be found from Fig. 19(b)–(d) that the dq0-axis currents can all track their respective references precisely during the mode switching. Since the proposed FC voltage regulation strategy is decoupled with the speed closed-loop control, the real-time speed and torque are stable during the mode switching process, as shown in Fig. 19(e). Fig. 19 proves the effective FC voltage regulation and smooth mode switching of the proposed strategy.

Fig. 20 shows comparison of the maximum speeds of hybrid-inverter mode and common dc-bus mode with 100-V dc source and no load. Instead of using speed closed-loop control, the drive operates in the respective modulation upper limits of 2:1 in hybrid-inverter mode and 1:1 in common dc-bus mode to compare their maximum speeds under limited dc source voltage. It can be seen from Fig. 20 that the maximum speed increases from 495 r/min in the hybrid-inverter mode to 940 r/min in the common dc-bus mode with an increment of 89.90%, which proves that the drive in common dc-bus mode has a wider speed range than that in hybrid-inverter mode.

The fault-tolerant control of Phase-A open-phase fault under 500 r/min speed and 5-Nm load are shown in Fig. 21. Due to the

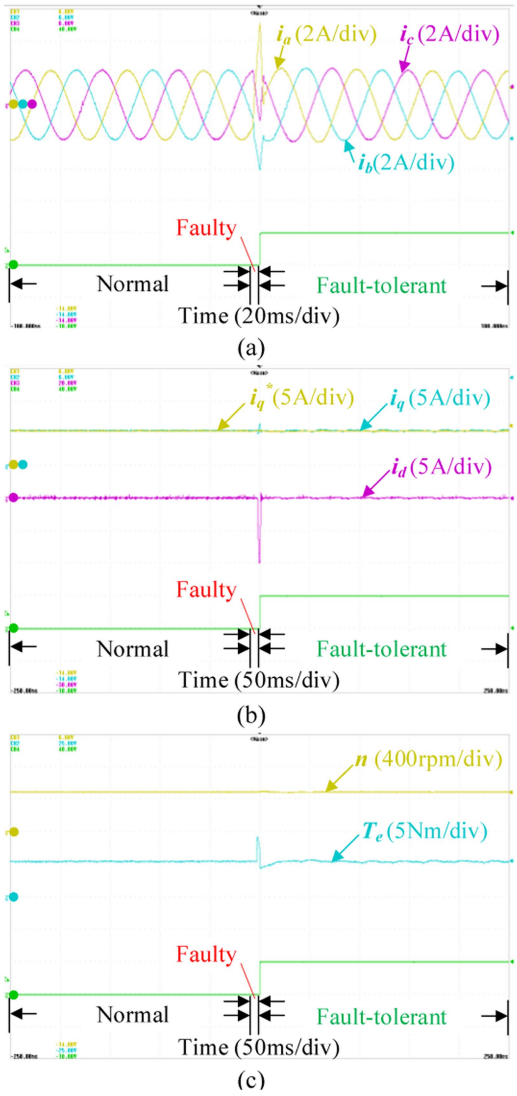

Fig. 23. Fault-tolerant control for S_{11} short-circuit fault. (a) Three-phase currents. (b) d-axis and q-axis currents. (c) Speed and torque.

Phase-A open circuit, i_a remains zero in Fig. 21(a). The distorted currents i_b and i_c become sinusoidal after the fault-tolerant strategy is applied. Moreover, the large current tracking errors in the $dq0$-axis currents are all eliminated and the torque fluctuation is suppressed by injecting the sinusoidal ZSC deduced in (8), as shown in Fig. 21(b)–(d).

The fault-tolerant operation of open-switch fault under 500 r/min speed and 5-Nm load is shown in Fig. 22. To better validate the proposed modulation strategy, a constant q-axis current reference is used. It can be seen from Fig. 22(a)–(b) that the phase currents recover quickly and the dq-axis currents track their corresponding references successfully in the fault-tolerant operation. In Fig. 22(c), the large torque ripple is eliminated after fault tolerance. The results in Fig. 22 prove effectiveness of the proposed fault-tolerant scheme for open-switch fault.

The fault-tolerant operation of the short-switch fault under 500 r/min speed and 5-Nm load is shown in Fig. 23. When a short-switch fault occurs, the currents will increase rapidly. For safety reasons, a current threshold is set to trigger the fault-tolerant control. The pulses in the middle of Fig. 23(a)–(c) are caused by S_{11} short-circuit fault. It can be found from Fig. 23 that the phase currents and the dq-axis currents can track their references, and the speed and torque return to normal after fault-tolerant control is introduced. The results in Fig. 23 illustrate a well-performed fault-tolerant control of the short-switch fault.

VI. Conclusion

This article proposed a two-mode inverter-based OW-PMSM drive and its modulation strategies, which has the hybrid-inverter mode and common dc-bus mode. In hybrid-inverter mode, high power quality can be achieved at the voltage ratio of 2:1, and a modulation strategy for any voltage ratio was proposed to make the voltage ratio vary more flexibly and precisely, leading to the smooth zero FC voltage starting and mode switching. In the common dc-bus mode, the speed range of the system was increased by nearly 90% in the experiment compared with the hybrid-inverter mode. Besides, the proposed two-mode inverter-based drive could switch into a proper mode to handle open-phase faults and switch faults effectively. In this article, the high power quality of the voltage ratio 2:1 and the high reliability of the voltage ratio 1:1 were combined to fully exploit the potential of the OW-PMSM drive.

References

[1] X. Wang et al., "Fault-tolerant control of common electrical faults in dual three-phase PMSM drives fed by T-type three-level inverters," *IEEE Trans. Ind. Appl.*, vol. 57, no. 1, pp. 481–491, Jan./Feb. 2021.

[2] K. T. Chau, C. C. Chan, and C. Liu, "Overview of permanent-magnet brushless drives for electric and hybrid electric vehicles," *IEEE Trans. Ind. Electron.*, vol. 55, no. 6, pp. 2246–2257, Jun. 2008.

[3] Y. Zhang, Y. Mao, X. Wang, Z. Wang, D. Xiao, and G. Fang, "Current prediction-based fast diagnosis of electrical faults in PMSM drives," *IEEE Trans. Transp. Electrific.*, vol. 8, no. 4, pp. 4622–4632, Dec. 2022.

[4] W. Hu, C. Ruan, H. Nian, and D. Sun, "Zero-sequence current suppression strategy with common-mode voltage control for open-end winding PMSM drives with common DC bus," *IEEE Trans. Ind. Electron.*, vol. 68, no. 6, pp. 4691–4702, Jun. 2021.

[5] M. S. R. Saeed, W. Song, B. Yu, Z. Xie, and X. Feng, "Low-complexity deadbeat model predictive current control for open-winding PMSM drive with zero-sequence current suppression," *IEEE Trans. Transp. Electrific.*, vol. 7, no. 4, pp. 2671–2682, Dec. 2021.

[6] M. Wang, D. Sun, W. Ke, and H. Nian, "A universal lookup table-based direct torque control for OW-PMSM drives," *IEEE Trans. Power Electron.*, vol. 36, no. 6, pp. 6188–6191, Jun. 2021.

[7] Z. Huang, T. Yang, P. Giangrande, M. Galea, and P. Wheeler, "Technical review of dual inverter topologies for more electric aircraft applications," *IEEE Trans. Transp. Electrific.*, vol. 8, no. 2, pp. 1966–1980, Jun. 2022.

[8] A. Somani, R. K. Gupta, K. K. Mohapatra, and N. Mohan, "On the causes of circulating currents in PWM drives with open-end winding AC machines," *IEEE Trans. Ind. Electron.*, vol. 60, no. 9, pp. 3670–3678, Sep. 2013.

[9] L. Cheng, H. Jianhui, and S. Jing, "Dual-vector predictive current control of open-end winding PMSM with zero-sequence current hysteresis control," *IEEE J. Emerg. Sel. Top. Power Electron.*, vol. 10, no. 1, pp. 184–195, Feb. 2022.

[10] Y. Zuo, X. Zhu, X. Si, and C. H. T. Lee, "Fault-tolerant control for multiple open-leg faults in open-end winding permanent magnet synchronous motor system based on winding reconnection," *IEEE Trans. Power Electron.*, vol. 36, no. 5, pp. 6068–6078, May 2021.

[11] S. Lakhimsetty, N. Surulivel, and V. T. Somasekhar, "Improvised SVPWM strategies for an enhanced performance for a four-level open-end winding induction motor drive," *IEEE Trans. Ind. Electron.*, vol. 64, no. 4, pp. 2750–2759, Apr. 2017.
[12] D. Sun, Z. Zheng, B. Lin, W. Zhou, and M. Chen, "A hybrid PWM-based field weakening strategy for a hybrid-inverter-driven open-winding PMSM system," *IEEE Trans. Energy Convers.*, vol. 32, no. 3, pp. 857–865, Sep. 2017.
[13] S. Chowdhury, P. W. Wheeler, C. Patel, and C. Gerada, "A multilevel converter with a floating bridge for open-end winding motor drive applications," *IEEE Trans. Ind. Electron.*, vol. 63, no. 9, pp. 5366–5375, Sep. 2016.
[14] Z. Huang, T. Yang, P. Giangrande, S. Chowdhury, M. Galea, and P. Wheeler, "An active modulation scheme to boost voltage utilization of the dual converter with a floating bridge," *IEEE Trans. Ind. Electron.*, vol. 66, no. 7, pp. 5623–5633, Jul. 2019.
[15] L. Chu et al., "Research on control strategies of an open-end winding permanent magnet synchronous driving motor (OW-PMSM)-equipped dual inverter with a switchable winding mode for electric vehicles," *Energies*, vol. 10, no. 5, May 2017, Art. no. 616.
[16] W. Hu, H. Nian, and D. Sun, "Zero-sequence current suppression strategy with reduced switching frequency for open-end winding PMSM drives with common DC Bus," *IEEE Trans. Ind. Electron.*, vol. 66, no. 10, pp. 7613–7623, Oct. 2019.
[17] C. Zhang et al., "Zero-sequence current suppression method for fault-tolerant OW-PMSM drive with asymmetric zero-sequence voltage injection," *IEEE Trans. Ind. Electron.*, vol. 70, no. 3, pp. 2351–2362, Mar. 2023.
[18] R. E. Kodumur Meesala, V. P. K. Kunisetti, and V. Kumar Thippiripati, "Enhanced predictive torque control for open end winding induction motor drive without weighting factor assignment," *IEEE Trans. Power Electron.*, vol. 34, no. 1, pp. 503–513, Jan. 2019.
[19] S. Chowdhury, P. Wheeler, C. Gerada, and C. Patel, "A dual two-level inverter with a single source for open end winding induction motor drive application," in *Proc. 17th Eur. Conf. Power Electron. Appl.*, 2015, pp. 1–9.
[20] B. V. Reddy and V. T. Somasekhar, "A dual inverter fed four-level open-end winding induction motor drive with a nested rectifier-inverter," *IEEE Trans. Ind. Inform.*, vol. 9, no. 2, pp. 938–946, May 2013.
[21] S. Lakhimsetty and V. T. Somasekhar, "An efficient predictive current control strategy for a four-level open-end winding induction motor drive," *IEEE Trans. Power Electron.*, vol. 35, no. 6, pp. 6198–6207, Jun. 2020.
[22] Z. Huang, T. Yang, P. Giangrande, S. Chowdhury, M. Galea, and P. Wheeler, "Enhanced performance of dual inverter with a floating capacitor for motor drive applications," *IEEE Trans. Power Electron.*, vol. 36, no. 6, pp. 6903–6916, Jun. 2021.
[23] W. Hu, C. Ruan, H. Nian, and D. Sun, "Simplified modulation scheme for open-end winding PMSM system with common DC bus under open-phase fault based on circulating current suppression," *IEEE Trans. Power Electron.*, vol. 35, no. 1, pp. 10–14, Jan. 2020.
[24] W. Chen, D. Sun, M. Wang, and H. Nian, "Modeling and control for open-winding PMSM under open-phase fault based on new coordinate transformations," *IEEE Trans. Power Electron.*, vol. 36, no. 6, pp. 6892–6902, Jun. 2021.
[25] Z. Song, F. Zhou, Y. Yu, R. Zhang, and S. Hu, "Open-phase fault-tolerant predictive control strategy for open-end-winding permanent magnet synchronous machines without postfault controller reconfiguration," *IEEE Trans. Ind. Electron.*, vol. 68, no. 5, pp. 3770–3781, May 2021.
[26] N. Chai and W. Hu, "A fault-tolerant scheme against the open-switch failure in open-end winding PMSM system with isolated DC bus," *IEEE Trans. Energy Convers.*, to be published, doi: 10.1109/TEC.2021.3115975.
[27] W. Zhao, B. Wu, Q. Chen, and J. Zhu, "Fault-tolerant direct thrust force control for a dual inverter fed open-end winding linear vernier permanent-magnet motor using improved SVPWM," *IEEE Trans. Ind. Electron.*, vol. 65, no. 9, pp. 7458–7467, Sep. 2018.
[28] W. Zhou, D. Sun, M. Chen, and B. Lin, "Simplified PWM for fault tolerant control of open winding PMSM fed by hybrid inverter," in *Proc. IEEE Energy Convers. Congr. Expo.*, 2015, pp. 2912–2918.

Tao Xu (Student Member, IEEE) received the B.S. degree in electrical engineering from Sichuan University, Chengdu, China, in 2022. He is currently working toward the M.S. in electrical engineering from Southeast University, Nanjing, China.

His research interests include the control of open-winding permanent magnet synchronous motors and multilevel PWM strategy.

Xueqing Wang (Member, IEEE) received the B.S. degree in electrical engineering from Tianjin University of Science and Technology, Tianjin, China, in 2014, and the M.S. and Ph.D. degrees from Southeast University, Nanjing, China, in 2016 and 2020, respectively, both in electrical engineering. From 2018 to 2019, he was a joint Ph.D. with McMaster Automotive Resource Centre, McMaster University, Hamilton, ON, Canada.

He is currently an Associate Research Fellow with the College of Electrical Engineering, Sichuan University, Chengdu, China. His research interests include control of multiphase motor and open-winding motor, fault diagnosis and tolerant control of motor drive, and multilevel PWM strategy.

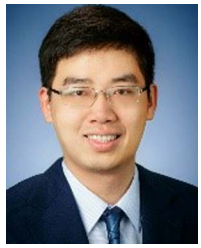

Dianxun Xiao (Member, IEEE) received the B.S and M.S degrees in electrical engineering from the Harbin Institute of Technology, Harbin, China, in 2016 and 2018, respectively, and the Ph.D. degree in electrical and computer engineering from McMaster University, Hamilton, ON, Canada, in 2021.

He is currently an Assistant Professor with the Sustainable Energy and Environment Thrust, The Hong Kong University of Science and Technology (Guangzhou), Guangzhou, China. Before that, he was a Postdoctoral Research Fellow with McMaster Automotive Resource Centre, McMaster University, in 2021.

His research interests include permanent magnet synchronous motor drives, switched reluctance motor drives, high-power converters, and battery management systems for transportation electrification applications.

Dr. Xiao is an Associate Editor for IEEE TRANSACTIONS ON TRANSPORTATION ELECTRIFICATION.

Xin Meng (Member, IEEE) received the B.S. degree from University of Electronic Science and Technology of China (UESTC), Chengdu, China, and the Ph.D. degree from Xi' an Jiaotong University (XJTU), Xi' an, China, in 2014 and 2019, respectively, all in electrical engineering.

He then joined Electrical Engineering School, Sichuan University, Chengdu, China, as a Faculty Member. His research interests include the control of parallel three phase inverters for uninterrupted power supply and micro-grid application, such as VSG control, droop control and seamless transfer between grid-connected mode and islanding mode.

Yao Mao (Member, IEEE) received the B.S. degree in automatic control from Chongqing University, Chongqing, China, in 2001, and the Ph.D. degree in signal and information processing from the Institute of Optics and Electronics, Chinese Academy of Sciences, Beijing, China, in 2012.

He has been a Professor with the University of Chinese Academy of Sciences since 2016. His research interests include power electronics, motion control, information fusion, and machine learning.

Dr. Mao was the recipient of the honored Distinguished Scientific Achievement Award by the Chinese Academy of Science in 2011.

Zheng Wang (Senior Member, IEEE) received the B.Eng. and M.Eng. degrees from Southeast University, Nanjing, China, in 2000 and 2003, respectively, and the Ph.D. degree from The University of Hong Kong, Hong Kong, in 2008, all in electrical engineering.

From 2008 to 2009, he was a Postdoctoral Fellow with Ryerson University, Toronto, ON, Canada. He is currently a full Professor with the School of Electrical Engineering, Southeast University. He has authored or coauthored over 80 internationally refereed papers and four books in these areas. His research interests include electric drives, power electronics, and distributed generation.

Dr. Wang was the recipient of several academic awards including IEEE PES Chapter Outstanding Engineer Award, Best Paper Award of International Conference on Electrical Machines and Systems (ICMES), Best Session Paper Award of IEEE Annual Meeting of Industrial Electronics (IECON), and Nanjing Outstanding Paper Award of Natural Science.